

Cite this: *J. Mater. Chem. A*, 2025, 13, 17590

Enhanced direct air capture by uranyl superoxide: a comprehensive study of the carbonation reaction of uranyl peroxide complexes†

Sarah K. Scherrer  and Tori Z. Forbes *

Reactive oxygen species, such as superoxide, are known to engage in direct air carbon capture within strong base systems. Previous work has also suggested that U(VI) peroxide/superoxide solids may also engage in this process, although the phase behavior and kinetics of this system have not been explored. Herein, we report optimal conditions which promote carbonation of two potassium uranyl triperoxide phases and their analogous diperoxo superoxide forms. Raman spectroscopy and elemental analysis were used to monitor the carbonation reaction, and the data was subjected to Principal Component Analysis (PCA) to gain insight on the complex reactivity of these phases. These systems exhibited full carbon dioxide (CO₂) uptake at 22 °C when relative humidity is at least 45%. Further, carbonation of the uranyl peroxide complexes occurred under atmospherically relevant CO₂ concentrations, and we utilized a custom-built reaction chamber to evaluate the kinetics of this process. Our results identified conditions favoring the carbonation of uranyl peroxide complexes and provide insight on the mechanism of carbonate formation.

Received 6th March 2025
Accepted 24th April 2025

DOI: 10.1039/d5ta01836f

rsc.li/materials-a

Introduction

Carbon negative methods are employed to remove atmospheric carbon dioxide (CO₂) for permanent storage or transformation into chemical species, such as carbonate (CO₃²⁻).¹⁻³ The most promising carbon negative technique is direct air capture (DAC), which utilizes a chemical sorbent to selectively bind CO₂ in air.⁴⁻⁶ Solid or liquid amines (*e.g.*, monoethanolamine (MEA))⁷⁻¹¹ and aqueous strong base (*e.g.*, potassium hydroxide (KOH) or sodium hydroxide (NaOH))^{6,12-16} are the most established DAC sorbents; however, these methods are currently energy intensive and economically challenging.^{4,5,17-19} Specifically, these sorbents are limited by slow kinetics due to ultra-dilute CO₂ concentration in ambient air (approximately 420 ppm (*ref.* 20)). Thus, there is a critical need for novel and cost-effective DAC materials and methods to achieve gigaton scale removal.

Previous work has demonstrated full mineralization or conversion of CO₂ from metal (*i.e.*, Na⁺, K⁺) stabilized reactive oxygen species (ROS) such as peroxide (O₂²⁻) and superoxide (O₂⁻), but fundamental challenges within ROS-based carbon capture persist.²¹⁻³¹ Most significantly, ROS are known to rapidly decompose in the presence of water, and large volumes of highly concentrated (9.25 M) hydrogen peroxide (H₂O₂) are necessary to remain competitive with established methods.

Stoin *et al.*²¹ have reported both superior efficiency of CO₂ removal and improved kinetics *via* mixed solutions of alkali hydroxides and H₂O₂ with the *in situ* generation of O₂⁻ inducing enhanced reactivity. However, this work identified a crucial limitation in that H₂O₂ spontaneously decomposes in alkaline conditions, thus hindering its overall efficiency without the addition of a chemical stabilizer such as sodium pyrophosphate. More recently, Ribó *et al.*²³ described the reaction between vanadium peroxides (with small amounts of O₂⁻ detected) and atmospheric CO₂; however, major challenges remain for these materials in that they can undergo auto-decomposition under air instead of reacting with CO₂. Additionally, they exhibit slow kinetics for the carbonation reaction with full conversion requiring several months in ambient air. Kravchuk *et al.*³² previously reported that U(VI) also stabilizes O₂⁻ within a potassium uranyl peroxide/superoxide complex (KUPS-1) K_{4-x}[UO₂(O₂)_{3-x}(O₂⁻)_x](H₂O)₄(H₂O)₄ (0 < x ≤ 1) which exhibited reactivity with atmospheric CO₂ forming uranyl carbonate phases, K₄[(UO₂)(O₂)(CO₃)₂]·xH₂O (x = 1, 2.5) and K₄[(UO₂)(CO₃)₃] (Fig. 1). This work also suggested that use of radical initiators such as benzaldehyde may reduce necessary H₂O₂ input by 90%.^{32,33} More recently, Scherrer *et al.*³⁴ demonstrated that the material initially forms as potassium uranyl triperoxide (KUT-1) K₄[UO₂(O₂)₃](H₂O)₄(H₂O)₄ with oxidation of O₂²⁻ to O₂⁻ occurring in the solid-state material within 3 weeks under inert conditions. In aqueous media, this process occurred within 48 hours and enhanced water stability of O₂⁻ coordinated to U(VI) was observed. These studies also found that the KUT-1 phase is a precursor to the potassium uranyl triperoxide (KUT, K₄[UO₂(O₂)₃]·4H₂O) reported by Dembowski *et al.*³⁵

Department of Chemistry, University of Iowa, Iowa City, Iowa 52242, USA. E-mail: tori-forbes@uiowa.edu† Electronic supplementary information (ESI) available. See DOI: <https://doi.org/10.1039/d5ta01836f>

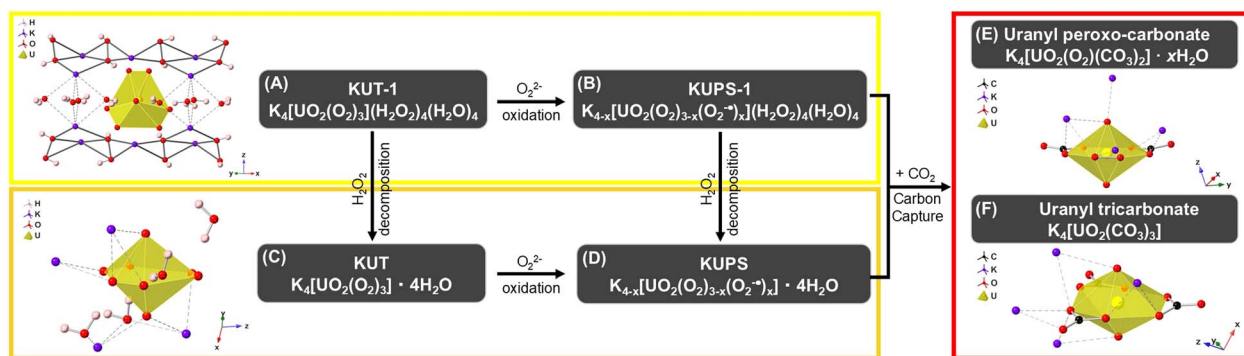


Fig. 1 Conversion of (A) KUT-1 to (B) KUPS-1 following O_2^{2-} oxidation or to (C) KUT following decomposition of H_2O_2 within the K^+ network. (D) KUPS is formed after H_2O_2 decomposition of (B) or O_2^{2-} oxidation of (C). Upon exposure to atmospheric CO_2 , the superoxide containing materials undergo direct air carbon capture to form uranyl carbonate phases ((E) uranyl peroxy-carbonate and (F) uranyl tricarbonate).

KUT-1 and KUT phases are differentiated by their respective lattices where KUT-1 contains a potassium network with coordinated H_2O_2 and aqua ligands, while KUT contains only potassium ions and lattice waters (Fig. 1). Both KUT and KUT-1 can undergo O_2^{2-} oxidation ultimately forming a uranyl diperoxo superoxide monomer in KUPS ($K_{4-x}[UO_2(O_2)_{3-x}(O_2^{\cdot-})_x] \cdot 4H_2O$, $0 < x \leq 1$) and KUPS-1, respectively, with interconversion of these materials illustrated in Fig. 1. While the KUPS-1 compound has previously shown spontaneous carbonation in the presence of air, the behavior of the other related compounds is unknown.

Herein, we investigated optimal conditions promoting the carbonation of KUT-1, KUT, KUPS-1, and KUPS within a custom-built flow-through apparatus using both high purity CO_2 and compressed air to mimic both point sources and direct air capture processes. Previous work noted that humid conditions influence the stability and efficiency of carbon capture sorbents, and ROS exhibit water sensitivity, which may lead to sorbent degradation and hinder carbonation.^{36–38} Hence, we explored carbonation in low, mid, and high relative humidity (RH) conditions. Elemental analysis, powder X-ray diffraction (PXRD), Raman spectroscopy, and electron paramagnetic resonance (EPR) spectroscopy were used to analyze the pure and reacted materials. Finally, the carbonation reaction kinetics for solid KUT-1, KUPS-1, KUT and KUPS were explored using a custom-built chamber equipped with a high sensitivity CO_2 sensor.

Experimental methods

Materials synthesis

All aqueous solutions were prepared using Millipore water (18.2 M Ω) and chemicals purchased were used directly without further purification. *Caution: $UO_2(NO_3)_2 \cdot 6H_2O$ contains radioactive ^{238}U , which is an α emitter, and like all radioactive materials must be handled with care. These experiments were conducted by trained personnel in a licensed research facility with special precautions taken toward the handling, monitoring, and disposal of radioactive materials.* KUT-1 was synthesized and isolated as previously reported.³⁴ To synthesize large quantities of material,

batches of at least 40 synthetic 20 mL vials were prepared with each containing 0.2 mL 0.05 M uranyl nitrate hexahydrate (International Bio-Analytical Industries Inc., 99.99%) in methanol, 0.15 mL pure methanol (Fischer Chemical, ACS 99.9%) and 2.5 mL benzyl alcohol (Alfa Aesar, 99%). A separate solution containing 0.2 mL 0.9 M aqueous potassium hydroxide (Sigma-Aldrich, 90%), 0.3 mL 0.05 M aqueous *N*-(phosphonomethyl) iminodiacetic acid hydrate (Sigma-Aldrich, 95%) with potassium hydroxide for solubility, and 0.2 mL 30% aqueous H_2O_2 (Fisher Chemical, ACS 99.9%) was mixed *via* vortex and carefully layered on top of the organic layer for each scintillation vial. The vials were capped and stored in the dark for overnight crystallization.

To isolate solid KUT-1, the contents of each scintillation vial were transferred to a 15 mL plastic conical tube and centrifuged at 5000 rpm for 5 minutes. Each conical tube was decanted followed by the addition of 5 mL methylene chloride (Fisher Chemical, >99.5%). Conical tubes were centrifuged for an additional 5 minutes at 5000 rpm ensuring any residual water was forced into the top aqueous layer. The aqueous layer was decanted and the KUT-1 solid was transferred to a watch glass for vacuum desiccator drying. Upon drying for a minimum of 20 minutes, the solid material was immediately utilized in the studies described herein. For the studies involving KUPS-1, the material was aged under argon gas. After about 3 weeks, the material was periodically checked for the presence of $O_2^{\cdot-}$ *via* EPR spectroscopy. Upon $O_2^{\cdot-}$ detection, materials were utilized or held under argon or vacuum. KUT-1 samples were characterized for purity using powder X-ray diffraction and Raman spectroscopy.

KUT was synthesized similarly to its previously reported protocol.³⁵ In a 20 mL scintillation vial, 2 mL 0.5 M uranyl nitrate hexahydrate, 2 mL 30% H_2O_2 and 2 mL 8 M KOH were mixed. Approximately 1 mL of pure methanol was added slowly. Scintillation vials were capped, and a yellow precipitant formed rapidly, typically within five minutes but could take several hours. The resulting solid was isolated *via* vacuum filtration, rinsed with methanol and dried. Any material that was not used immediately was stored under argon. Before using any of the additional material, samples were checked for $O_2^{\cdot-}$ *via* EPR



spectroscopy, and the purity was determined using X-ray diffraction and Raman spectroscopy. Studies involving KUPS utilized the material after detection of $O_2^{\cdot -}$ by EPR spectroscopy.

The uranyl peroxo-carbonate phase $K_4[UO_2(O_2)(CO_3)_2] \cdot 2.5H_2O$ was also synthesized to serve as a model carbonated compound using a method adapted from Zehnder *et al.*³⁹ and Goff *et al.*⁴⁰ For the modified synthesis, UO_2 powder was dissolved in 2 M K_2CO_3 and 30% H_2O_2 at room temperature. The solution was stirred for one hour and additional 30% H_2O_2 was added to the solution. Four mL aliquots of the solution were transferred to 20 mL scintillation vials and 6 mL methanol was layered onto the solution. The vials were capped and left to crystallize at room temperature in the dark overnight. Dark orange/red precipitate formed on the bottom of the vials and then the solid was vacuum filtered and dried. The resulting materials were characterized for purity using powder X-ray diffraction and Raman spectroscopy.

Details of reaction apparatus

Flow-through studies. A custom-built flow-through apparatus (ESI, Fig. S1†) was utilized to determine optimal conditions for carbonation of uranyl superoxide at 22 °C. The apparatus uses polytetrafluoroethylene (PTFE) tubing connected to a CO_2 gas cylinder (99.9%, Linde Air). The main CO_2 line is split into a dry gas line with an additional moisture scrubber and a line entering a humidity chamber. The humidity line is connected to a flowmeter for precise control of RH and two gas streams conjoin and connect to a flowmeter for flow rate control. A humidity sensor in the gas line allows for real-time temperature and humidity monitoring. The gas line is connected to three sample chambers, which are connected to a bubbler to prevent pressure build-up. All flow-through studies were performed in triplicate using 20 to 30 mg of material for 2 hours at a designated RH. Subsequent flow-through studies were performed in a similar manner with a compressed air gas cylinder (<1000 ppm CO_2 , Linde Air). Additionally, extended flow-through studies were completed with compressed air at 45% RH for approximately 24 hours. After completion of the experiments, the material was analyzed by Raman spectroscopy, powder X-ray diffraction, and combustion elemental analysis.

Batch studies. A custom-built reactor utilized for batch kinetics studies of all phases was constructed using an acrylic vacuum chamber with a removable top. The chamber was equipped with a Vaisala GMP343 CO_2 probe to measure CO_2 concentration with accuracy of ± 3 ppm, and an ALTA Wireless Humidity Sensor for relative humidity monitoring with accuracy of $\pm 2\%$ RH (ESI, Fig. S2†). Batch studies were conducted in triplicate for all materials. The chamber was opened and filled with ambient air and RH typically measured in the range of 40–50% throughout each batch study. Initial $[CO_2]$ ranged from 415–510 ppm and was monitored until equilibrium was reached. Background readings of the chamber filled with ambient air, argon and evacuated were collected for one-month durations to ensure no leaks within the system. A reference standard of potassium hydroxide was used as this translates to

the strong base sorbents already used in DAC processes. Materials were characterized after the reaction using powder X-ray diffraction, Raman spectroscopy, and combustion elemental analysis.

Characterization of the synthesized and reacted materials

Combustion elemental analysis. CHN Combustion Elemental Analysis was performed using the Exeter Analytical 440 Analyzer. Samples weighing 1500–1900 μg were prepared in tin capsules, sealed *via* crimping, and placed in nickel sleeves. For proper calibration at the beginning of each experiment, ACS grade acetonitrile was used as a conditioner and a standard. Sample collection was performed in triplicate in order of increasing carbon content. An additional blank and standard were run following every 10 samples to maintain accurate calibration. Lanthanum carbonate samples were included at the conclusion of every experiment for an additional reference standard. Following data collection, average CHN contents and their respective standard deviations were computed.

Powder X-ray diffraction. Powder X-ray diffraction data on the as synthesized and reacted materials was collected on a Bruker D8 Advance diffractometer with nickel filtered $Cu K\alpha$ radiation ($\lambda = 1.5418 \text{ \AA}$). Samples were ground to a fine powder in a mortar and pestle and loaded on the sample holder equipped with a zero-background silica plate. Voltage and current were set at 40 kV and 40 mA, respectively and the diffractogram was collected in the continuous mode scanning from $5\text{--}60^\circ 2\theta$ with a step size of 0.05° . Background subtraction was completed in PreDICT 64-bit software. Mercury was utilized to obtain the simulated powder patterns from reported crystal structures, which were then used for bulk phase identification.

Electron paramagnetic resonance spectroscopy. Solid-state continuous-wave X-band EPR spectroscopy was collected at room temperature using a Bruker Magnettech 5000 EPR spectrometer. Solid samples were loaded in a 200 mm \times 4 mm quartz EPR tube. Operating parameters (microwave power, modulation amplitude) were optimized for each sample. Modulation frequency was set to 100 kHz and frequency was 9.44 GHz. Magnetic field values were converted to *g*-factors and subsequent spectral analysis was performed using standard protocol. Data was plot in Origin 9.60 (OriginLab, Northampton, MA) 64-bit software.

Raman spectroscopy. Solid-state Raman spectroscopy was utilized for all samples prior to and at the conclusion of each flow-through experiment. Spectra were acquired on a SnRI High-Resolution Sierra 2.0 Raman Spectrometer equipped with a 785 nm laser and 2048 pixels TE-cooled detector. All spectra were acquired in three iterations with maximum laser energy of 15 mW for optimal resolution (2 cm^{-1}) and an integration time ranging from 2 to 30 seconds. Three iterations per sample were averaged and normalized by the appropriate laser power and integration time. Background subtraction was completed using PreDICT 64-bit software and peak fitting and analysis were performed in Origin 9.60 (OriginLab, Northampton, MA) 64-bit software using Lorentzian function peak analysis protocols.



Principal Component Analysis (PCA) was implemented for further interpretation of the Raman spectral data in Origin 9.60 (OriginLab, Northampton, MA) 64-bit software PCA app.⁴¹ Normalized and background subtracted data was utilized with each wavenumber (2000–200 cm⁻¹) representing the observations and the spectral intensities as the input data. The covariance matrix setting was used, and basic statistics, loadings, and scores were computed for each analysis. The number of significant principal components (PCs) was selected based on the number of components explaining a minimum of 95% total variance. Resulting calculations were plotted in either 2D or 3D, corresponding to the number of significant principal components.

Results and discussion

Confirmation of purity for the starting materials

Prior to flow-through experiments, materials characterization was performed on the as-synthesized materials (KUT-1, KUPS-1, KUT, and KUPS) and K₄[UO₂(O₂)(CO₃)₂].2.5H₂O to serve as references. PXRD patterns of the synthesized materials matched well with patterns simulated from single-crystal X-ray diffraction data (KUT-1/KUPS-1 ICSD 135984, KUT/KUPS ICSD 243360, K₄[UO₂(O₂)(CO₃)₂].2.5H₂O ICSD 173289 and K₄[UO₂(O₂)(CO₃)₂].H₂O ICSD 59925) indicating purity of the bulk phase (ESI, Fig. S3–S7†).

EPR spectroscopy was collected for the synthesized materials to confirm the absence/presence of O₂^{-•} (ESI, Fig. S8–S11†). Predicted features for O₂^{-•} in KUPS-1 are observed at $g_{\parallel} = 2.057$ and $g_{\perp} = 2.017$ ($g_x = 2.016$, $g_y = 2.017$, $g_z = 2.057$).³⁴ The predicted EPR spectrum of KUPS has yet to be reported, though the principal g -factors are presumably the same given the structural similarities with KUPS-1 specifically regarding the uranyl monomeric unit. Experimentally observed values are consistent with the predicted features for both KUPS-1 ($g_{\parallel} = 2.056$ and $g_{\perp} = 2.014$) and KUPS ($g_{\parallel} = 2.057$ and $g_{\perp} = 2.014$). The additional feature at $g = 2.037$ observed in the KUPS EPR spectrum could correspond to the g_{\parallel} of a second O₂^{-•} species, hence the apparent broadening of the $g_{\perp} = 2.014$ signature, however efforts to understand these interactions between paramagnetic species and U(vi) are ongoing. Lack of these features in the KUT-1 and KUT materials implies the presence of diamagnetic (EPR silent) O₂²⁻ within the triperoxide phases. Additional features observed in all materials are consistent with trace Cr(v) impurities that are known to exist within these materials.³⁴ The signature at $g = 1.982$ is consistent with the Cr(v)-peroxo complex [Cr(v)(O)(O₂)(OH₂)_x]⁺ and hyperfine splitting at $g = 1.994$ and $g = 1.953$.⁴² The isotropic feature at $g = 1.972$ also matches a Cr(v)-peroxo complex in the form of [Cr(v)(O₂)₄]³⁻.⁴²

Raman spectral features for all starting compounds were also collected and the features were analyzed to confirm vibrational modes (ESI, Fig. S12–S15†). Fitted spectrum of pure KUT-1 shows six bands in the spectroscopic window of interest and is well-aligned with previous reports of these phases.³² The highest intensity band at 727 cm⁻¹ corresponds to ν_1 symmetric stretch of UO₂²⁺.³² Bands at 812, 825, 849 and 880 cm⁻¹ correspond to ν_{1-3} motions of O₂²⁻ bound to UO₂²⁺.³⁵ The band

appearing at 860 cm⁻¹ corresponds to ν_{O-O} stretch of H₂O₂ coordinated to potassium within the potassium network.⁴³ Upon conversion to KUPS-1, the Raman features remain in the same range as in KUT-1 but do exhibit shifts related to the O₂²⁻ features (from 825 to 821 cm⁻¹) and ν_1 symmetric stretch of UO₂²⁺ (from 727 to 722 cm⁻¹). The fitted spectrum of KUT is quite similar with vibrational modes observed at 841, 822, and 811 cm⁻¹ for the ν_{1-3} motions of O₂²⁻ bound to UO₂²⁺ and 712 cm⁻¹ corresponding to the ν_1 UO₂²⁺ symmetric stretch. These features are in good agreement with those previously reported by Dembowski *et al.*³⁵ We note additional small features at about 1060 and 756 cm⁻¹ corresponding to surface CO₃²⁻ species.^{32,44} Efforts were taken to minimize the presence of any carbonate species in the starting materials, however given the highly reactive nature of these phases, they could not always be prevented from forming during sample transfer processes. When KUT transforms to the superoxide-containing phase KUPS, the Raman features only vary by 2–3 cm⁻¹, which is within error of the instrument.

The uranyl peroxo-carbonate K₄[UO₂(O₂)(CO₃)₂].2.5H₂O (ESI, Fig. S16†) model compound shows several distinct features in its vibrational spectrum. Most notably are the appearance of three bands at 1065, 1053 and 1030 cm⁻¹ indicative of CO₃²⁻ species, in addition to the most intense signal at 767 cm⁻¹ corresponding to ν_1 UO₂²⁺. Lower intensity bands at 693 and 716 cm⁻¹ (CO₃²⁻) and 806 cm⁻¹ (UO₂²⁺) are also identified. The remaining features at 840 and 850 cm⁻¹ correspond to O₂²⁻ bound to UO₂²⁺. The Raman spectrum of K₄[UO₂(O₂)(CO₃)₂].2.5H₂O is well aligned with the previously published spectrum.⁴⁰ Spectral assignments are summarized in Table 1.

To quantitatively assess the carbonation of KUT-1, KUPS-1, KUT and KUPS, we also performed CHN elemental analysis on the as synthesized samples to determine the amount of CO₂ captured by the material. On average, the pristine materials contained 0.045–0.095% carbon, or 0.027–0.057 mol C per mol U, confirming maximum purity. Average carbon contents for the KUT-1, KUPS-1, KUT and KUPS flow-through studies can be found in the ESI section (ESI, Table S1†).

Quantification of CO₂ capture. Visual changes (*i.e.*, color, morphology) to the samples are observed throughout the carbonation reaction indicating changes in the overall phase. Pristine KUT-1 and KUPS-1 are dry, bright yellow powders, while pristine KUT and KUPS are orangish-yellow in color. Upon exposure to CO₂ and different relative humidity values, significant visual changes occur. The materials darken throughout carbonation until the bright red/orange K₄[UO₂(O₂)(CO₃)₂].*x*H₂O ($x = 1, 2.5$) is formed. Morphology of the reacted material is highly dependent on relative humidity with the materials forming a hygroscopic slurry as RH increases.

Following flow-through experiments of KUT-1 with pure CO₂, amounts of carbon detected were highly dependent on the relative humidity throughout gas exposure (Fig. 2a). At 15% RH, the material contained an average of 0.207% carbon (0.125 mol C per mol U). Given the small change in the carbon content, we hypothesized that the detected carbon is primarily adsorbed CO₂. When RH is increased to 45% and 70% throughout CO₂



Table 1 Raman spectral assignments of the observed vibrational bands for KUT-1, KUPS-1, KUT, KUPS, and potassium uranyl peroxy-carbonate (UPDC) within the spectral window of interest (1200–600 cm^{-1})

KUT-1	KUPS-1	KUT	KUPS	UPDC	Assignment
				1065	$\nu_{\text{C-O}}$ for CO_3^{2-}
				1052	$\nu_{\text{C-O}}$ for CO_3^{2-}
				1029	$\nu_{\text{C-O}}$ for CO_3^{2-}
880	880				$\nu_{\text{O-O}}$ for H_2O_2 within lattice
860	868				$\nu_{\text{O-O}}$ stretch for H_2O_2 within lattice
849	848			850	ν_{1-3} for O_2^{2-} bound to UO_2^{2+}
		841	844	840	ν_{1-3} for O_2^{2-} bound to UO_2^{2+}
825	821	822	826		ν_{1-3} for O_2^{2-} bound to UO_2^{2+}
812	800	811	814	806	ν_{1-3} for O_2^{2-} bound to UO_2^{2+}
727	722	712	715	767	ν_1 for UO_2^{2+}
				716	$\nu_{\text{C-O}}$ for CO_3^{2-}
				692	$\nu_{\text{C-O}}$ for CO_3^{2-}

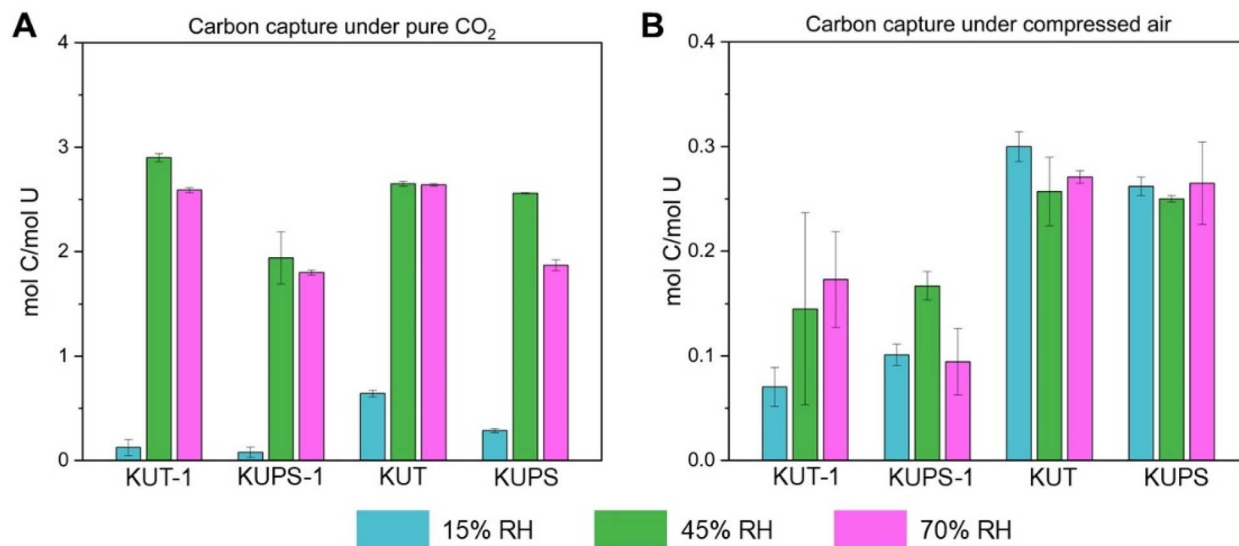
exposure, the average carbon contents of the materials were 4.800% (2.896 mol C per mol U) and 4.290% (2.588 mol C per mol U) respectively, suggesting conversion of KUT-1 to $\text{K}_4[\text{UO}_2(\text{O}_2)(\text{CO}_3)_2] \cdot \text{H}_2\text{O}$ (theoretical 4.025% C) or $\text{K}_4[\text{UO}_2(\text{O}_2)(\text{CO}_3)_2] \cdot 2.5\text{H}_2\text{O}$ (theoretical 3.850% C), and likely small amounts of $\text{K}_4[\text{UO}_2(\text{CO}_3)_3]$ (theoretical 5.936% C) or other carbonate rich phases (*i.e.*, K_2CO_3 , theoretical 8.683% C).

Flow-through experiments of KUT-1 with compressed air similarly suggest dependence on relative humidity, while additionally revealing the significance of CO_2 concentration (Fig. 2b). Samples at 15%, 45% and 70% RH were found to contain 0.117% (0.07 mol C per mol U), 0.240% (0.145 mol C per mol U) and 0.287% carbon (0.173 mol C per mol U), respectively. Therefore, negligible carbonation of KUT-1 occurs under ambient CO_2 concentrations in the two hours of air exposure.

Similar trends were observed in flow-through experiments with KUPS-1, KUT and KUPS, such that optimal carbonation

occurs at higher relative humidity and higher CO_2 content. Both KUT and KUPS exposed to pure CO_2 showed improved carbon capture at low relative humidity compared to KUT-1 and KUPS-1, though still significantly less than at higher RH. Carbon contents for KUPS-1 and KUPS exposed to ambient air in the flow-through system, regardless of RH, were comparable to that after pure CO_2 15% RH exposure. Following ambient air exposure across all RH values, KUT exhibited consistent carbon contents, which was over a 57% decrease in the carbon captured compared to low RH, pure CO_2 exposure. This implies that the presence of O_2^{2-} enhances the carbon capture reaction under ambient $[\text{CO}_2]$. It is highly likely that O_2^{2-} forms within the triperoxide phases as an intermediate step in the reaction mechanism, thus more CO_2 uptake is observed when the starting material already contains O_2^{2-} .

Both KUT and KUPS exhibit increased carbon capture under air at all relative humidity conditions compared to KUT-1 and KUPS-1. As outlined previously, the major difference between

**Fig. 2** Elemental analysis of KUT-1, KUPS-1, KUT and KUPS following flow-through studies at 15%, 45%, and 70% relative humidity under pure CO_2 (A) and compressed air (B).

these phases is the presence of H_2O_2 in the crystalline lattice for KUT-1/KUPS-1, which is absent for KUT/KUPS. Therefore, the $\text{K}^+/\text{H}_2\text{O}_2$ network in the KUT-1 and KUPS-1 compounds must impact the CO_2 absorption or reactivity, thus slowing down the process of CO_2 reacting with the uranyl peroxide monomer. However, the reasoning behind this change in reactivity was not clear, so we turned to vibrational analysis to understand changes in speciation throughout the process.

Vibrational and structural analysis for the carbonation reaction of KUT-1

Influence of relative humidity. Following 2 hours of CO_2 exposure at 15, 45 and 70% RH, Raman spectra were obtained, and the features were fit to further evaluate the overall changes. Flow-through studies at 15% RH yielded no substantial changes in the vibrational spectra or in the PXRD of the reacted material, indicating no carbonate formation (Fig. 3a and ESI Fig. S17†). This confirms the results from the elemental analysis suggesting that the detected carbon is primarily a small amount of adsorbed CO_2 . When RH is increased to 45 and 70%, the Raman spectra suggests that the peroxide within the lattice has reacted and overall, the $\text{U}(\text{vi})$ peroxo complex begins to convert to a uranyl peroxo-carbonate material (Fig. 3b and c).⁴⁰ Features associated with peroxide in the lattice (*i.e.*, 849, 860, and 880 cm^{-1}) are absent, indicating that the peroxide within the lattice has reacted under these higher relative humidity conditions. Ingrowth of vibrational bands at 1048 and 1031 cm^{-1} correspond to $\nu_1\text{ CO}_3^{2-}$ stretches that are bound to $\text{U}(\text{vi})$ as those associated with K_2CO_3 typically occur at 1067 cm^{-1} .⁴⁵ The highest intensity band at 800 cm^{-1} also aligns well with $\nu_1\text{ UO}_2^{2+}$ within uranyl carbonate complexes. Additional weaker bands at 677 and 636 cm^{-1} were also observed and are not typically

observed within solid-state carbonate materials. However, these features can be observed for ultra concentrated carbonate and bicarbonate solutions (3.5–8.0 M) and have been assigned to carbonate ion-water restricted rotations.⁴⁶ As the KUT-1 material absorbs a significant amount of water in the high RH environment, the presence of carbonate-ion water pairing is reasonable. In addition, a small feature at 1004 cm^{-1} is observed in the 70% RH sample. It could correspond to HCO_3^- as typical literature examples of HCO_3^- vibrational modes identify a $\nu_5\text{ C-OH}$ stretch at 1017 cm^{-1} .^{44,45} The slight redshift would imply secondary interactions within the coordinating environment; however, this assessment has not been fully confirmed. In general, the Raman spectra support that higher RH induces carbon capture with conversion of KUT-1 to a uranyl peroxo-carbonate phase. Lastly, bands at 828 , 817 , and 727 cm^{-1} remain and could correspond to the original material, indicating that not all the original KUT-1 has converted at this point.³² Bands at 817 and 727 cm^{-1} have also been correlated to $\nu_1\text{ UO}_2^{2+}$ bound to three CO_3^{2-} ligands and $\nu_1\text{ CO}_3^{2-}$ bound to U, respectively, which could indicate some degree of conversion to $\text{K}_4[\text{UO}_2(\text{CO}_3)_3]$.^{32,47} Given the viscous nature of the sample initially after the reaction at 45 and 70% RH, no PXRD data could be collected for these materials.

Additional transformation of the 45 and 70% RH samples were noted after being aged under ambient conditions for several days. Visually, the orange viscous material transformed to a dry red/orange powder over the course of three days in a sealed glass vial. The Raman spectrum revealed significant changes in the vibrational features, with bands at 1054 , 1050 , 850 , 840 , 790 , 768 , 714 , and 692 cm^{-1} , which are consistent with $\text{K}_4[\text{UO}_2(\text{O}_2)(\text{CO}_3)_2]\cdot 2.5\text{H}_2\text{O}$ (ESI, Fig. S18†).⁴⁰ Additional phase confirmation was

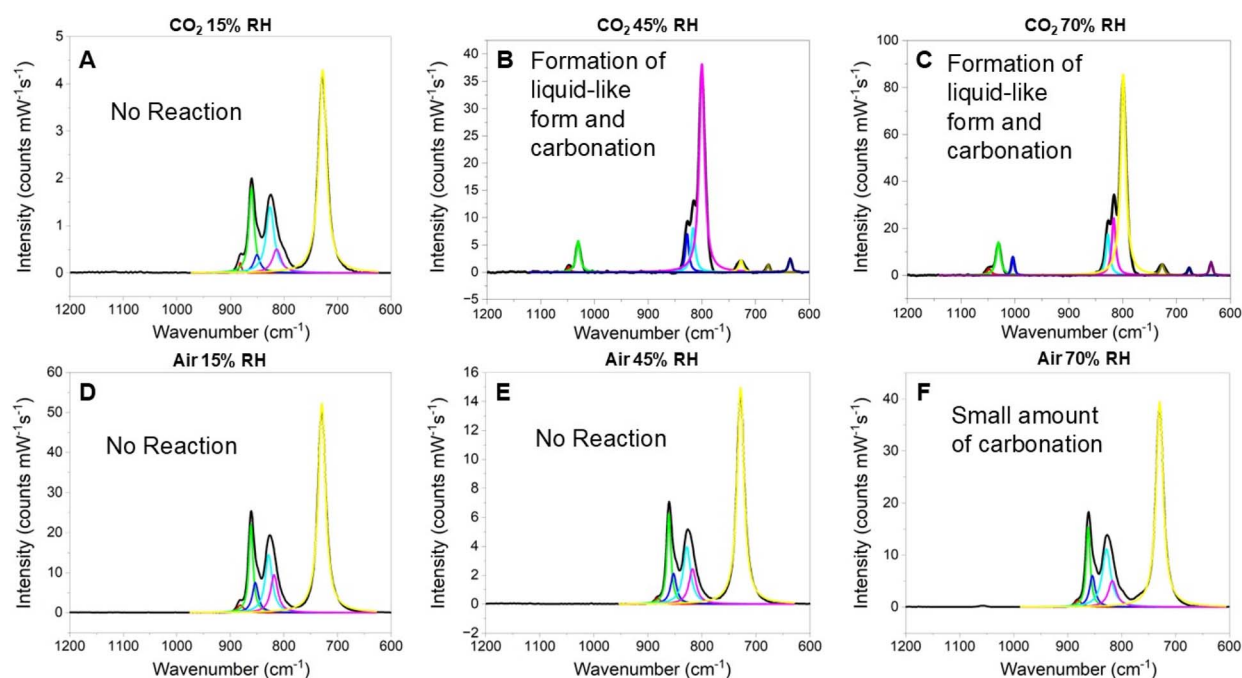


Fig. 3 Vibrational spectra following flow-through studies with KUT-1 exposed to pure CO_2 at (A) 15%, (B) 45% and (C) 70% RH. Vibrational spectra of KUT-1 following exposure to compressed air at 15%, 45% and 70% RH are shown as (D), (E), and (F), respectively.



provided by the PXRD of the dried powder, which confirmed the formation of crystalline $K_4[UO_2(O_2)(CO_3)_2] \cdot 2.5H_2O$ and $K_4[UO_2(CO_3)_3]$ (ESI, Fig. S19†). This further supports that the vibrational spectra of the samples immediately following flow-through experiments represent an intermediate phase in the carbonation reaction.

Influence of CO_2 concentration. After analysis of materials upon exposure to pure CO_2 , flow-through experiments were repeated utilizing compressed air at 15, 45 and 70% RH. Raman spectra of all samples are largely consistent with the starting KUT-1 material, suggesting that negligible carbonation occurred within the 2 hour period under ultra-dilute CO_2 concentrations (Fig. 3d–f). PXRD of the material after the 2 h reaction time also showed no changes from the initial material (ESI, Fig. S20†). Quantification of CO_2 captured (*vide supra*) suggests influence of RH even at low CO_2 concentrations, though much less pronounced. This implies that, while CO_2 concentration is the primary factor influencing the carbonation of KUT-1, reactivity is enhanced under higher RH. Additionally, we note that the EPR spectrum of KUT-1 following 2 hours of air exposure now reveals a small feature consistent with $O_2^{\cdot -}$ in KUPS-1 (ESI, Fig. S21†). This indicates rapid formation of $O_2^{\cdot -}$ under ambient conditions as previously noted and may contribute to the carbonation reaction mechanism.

Transformation of the samples exposed to compressed air was also observed after aging under ambient conditions for three days. The visual change was more subtle, with the yellow powders converting to a yellowish orange color, but numerous spectroscopic variations were noted for the vibrational features. Raman spectrum of the material three days after the exposure to

compressed air displayed vibrational modes at 844 ($\nu_1 O_2^{2-}$), 825 ($\nu_3 O_2^{2-}$), 814 ($\nu_2 O_2^{2-}$), and 716 ($\nu_1 UO_2^{2+}$) cm^{-1} consistent with that of KUT (ESI, Fig. S22†).³⁵ PXRD further confirms that the material converted to the KUT/KUPS phase (ESI, Fig. S23†) suggesting decomposition of the K^+/H_2O_2 network surrounding the uranyl monomer. Further transformation of the material was observed after three additional days sealed under ambient conditions with the vibrational spectrum and diffraction pattern suggesting conversion to $K_4[UO_2(O_2)(CO_3)_2] \cdot 2.5H_2O$ (ESI, Fig. S24 and S25†).⁴⁰ Presence of carbonation after the formation of $O_2^{\cdot -}$ within material suggests that the ROS species is a component of the reaction mechanism in the direct air carbon capture.

Vibrational and structural analysis for the carbonation reaction of KUPS-1, KUT and KUPS

Influence of superoxide and secondary coordination sphere. Flow-through studies varying the relative humidity, and the specific gas (CO_2 or compressed air) were repeated with KUPS-1 to gain additional insight on the influence of superoxide for the carbonation reaction. The vibrational spectra (Fig. 4) are largely consistent with those for KUT-1, although a feature, albeit very weak, at 1056 cm^{-1} is observed in all three of the samples exposed to compressed air. This supports the earlier statement from the elemental analysis data in that KUPS-1 exhibits enhanced carbon capture under dilute CO_2 concentrations. PXRD of the KUPS-1 samples exposed to air and CO_2 at 15% RH show features consistent with the starting material, in addition to new lower intensity features associated with UO_2CO_3 (ref. 48 and 49) (ESI, Fig. S26 and S27†). The KUPS-1 45% and 70% RH CO_2 spectra differ from those of KUT-1 in that many additional

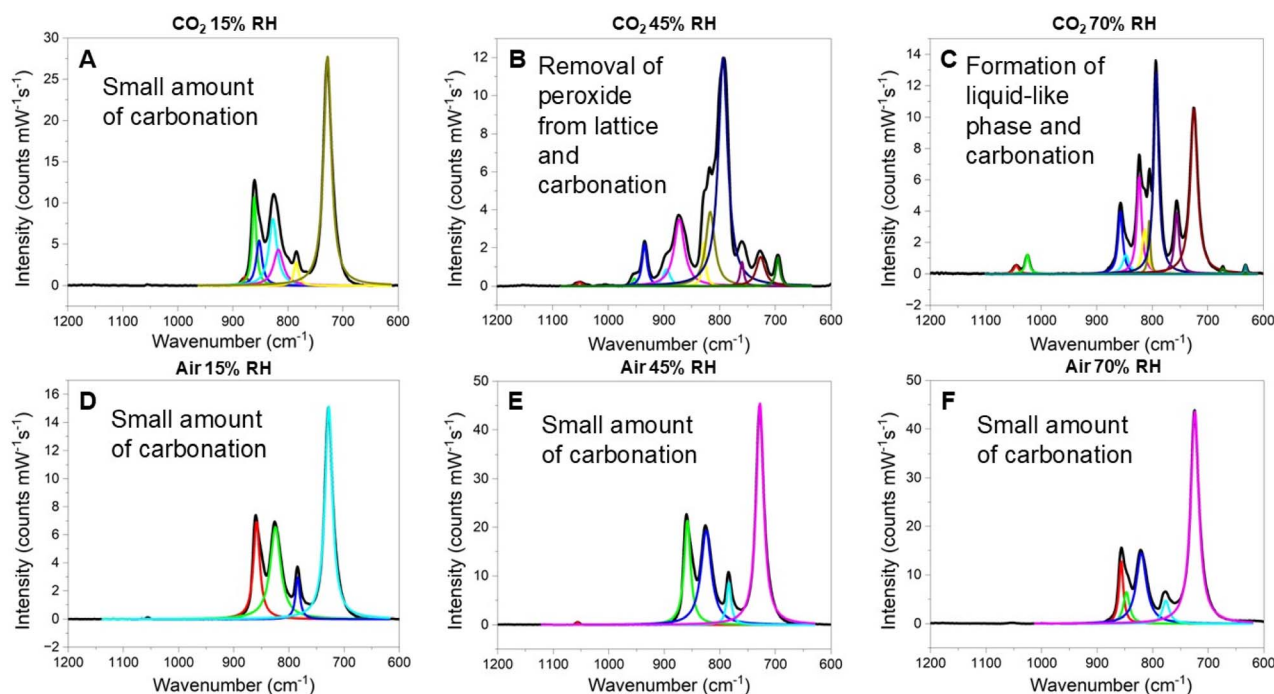


Fig. 4 Vibrational spectra following flow-through studies with KUPS-1 exposed to pure CO_2 at (A) 15%, (B) 45% and (C) 70% RH. Vibrational spectra of KUPS-1 following exposure to compressed air at 15%, 45% and 70% RH are shown as (D), (E), and (F), respectively.



features are observed in the window of interest. KUPS-1 exposed to pure CO₂ at 45% RH for two hours includes a band at 1052 cm⁻¹ that corresponds to a carbonate feature. In addition, there are bands at 953, 935 and 895 cm⁻¹ that are not observed in any other KUT-1 or KUPS-1 reacted samples. These bands cannot be definitively assigned, but features in that region were also noted by Mestl *et al.*⁵⁰ in the decomposition of BaO while heating and were attributed to non-crystalline peroxide species. Bands at 873, 828, 817, and 727 cm⁻¹ could correspond to residual KUPS-1 in the samples or to carbonate bound to U vibrations similar to those observed in reacted KUT-1.³² Given the spectral overlap, it is difficult to conclusively identify these features. When the samples are exposed to 70% RH, there are more residual uranyl triperoxide spectral signatures remaining in the sample, but we observe additional evidence of carbonation (bands at 1045 and 1025 cm⁻¹), including the formation of the uranyl tricarbonate complex (806 cm⁻¹ consistent with the reported U=O vibrational mode).⁵¹ Additionally, there is evidence that the hygroscopic sample becomes a concentrated liquid-like form, with features at 673 and 632 cm⁻¹. It is also important to point out the absence of features that would signify the formation of the uranyl peroxo-carbonate phase, particularly the peroxo stretches at 850 and 840 cm⁻¹ and the uranyl stretch at 767 cm⁻¹.

These studies were also repeated with KUT and KUPS to gain insight on the influence of changes in the secondary coordination sphere as both samples do not contain H₂O₂ coordinated to the K⁺ cations in the lattice (Fig. 5 and 6). The KUT sample contained a small amount of surface carbonate in the initial material so there was no significant reaction of the compound when exposed to compressed air. PXRD of the KUT materials following exposure to air indicate the remaining KUT phase, as

well as small features aligned with UO₂CO₃ (ESI, Fig. S28 and S29†). Under pure CO₂ at 15% RH, there was a second feature at 1055 cm⁻¹, as well as a feature at 766 cm⁻¹, suggesting that the formation of a small amount of the uranyl peroxo-carbonate.⁴⁰ In addition, there are features at 884 and 783 cm⁻¹ that match well with the formation of UO₂CO₃.^{48,49} The KUT vibrational features from the pristine material also blue shifted to those observed for the KUPS material, suggesting that the peroxide is beginning to oxidize. PXRD of the KUT compound exposed to CO₂ at 15% RH indicates that some KUT/KUPS remains crystalline, but there are also features that confirm a small amount of UO₂CO₃ in the sample (ESI, Fig. S30†). As the RH increases, the sample again absorbs a significant amount of water and the reactivity continues with carbonation (1047, 1029, and 635 cm⁻¹), reactive peroxide species (935 cm⁻¹), and free peroxide (875 cm⁻¹). This behavior continues as the RH increases to 70%. Reactivity is also observed for KUPS with a small amount of carbonation of the sample in air confirmed by PXRD (ESI, Fig. S31†) with the appearance of weak diffraction peaks associated with UO₂CO₃, which matches well with the elemental analysis. Similarly, some level of carbonation is observed for all KUPS samples that are exposed to CO₂, with additional uranyl carbonate features appearing with increasing relative humidity.

PCA-based spectral analysis. Due to complexity of the system, we employed Principal Component Analysis (PCA) on the Raman data to identify precise features unique to phases throughout the progression of the carbonation reaction and determine trends. The first PCA iteration included samples from flow-through studies with pure CO₂ and compressed air, aged samples, and K₄[UO₂(O₂)(CO₃)₂]·2.5H₂O associated with the KUT-1 materials. The loadings plot reveals three distinct

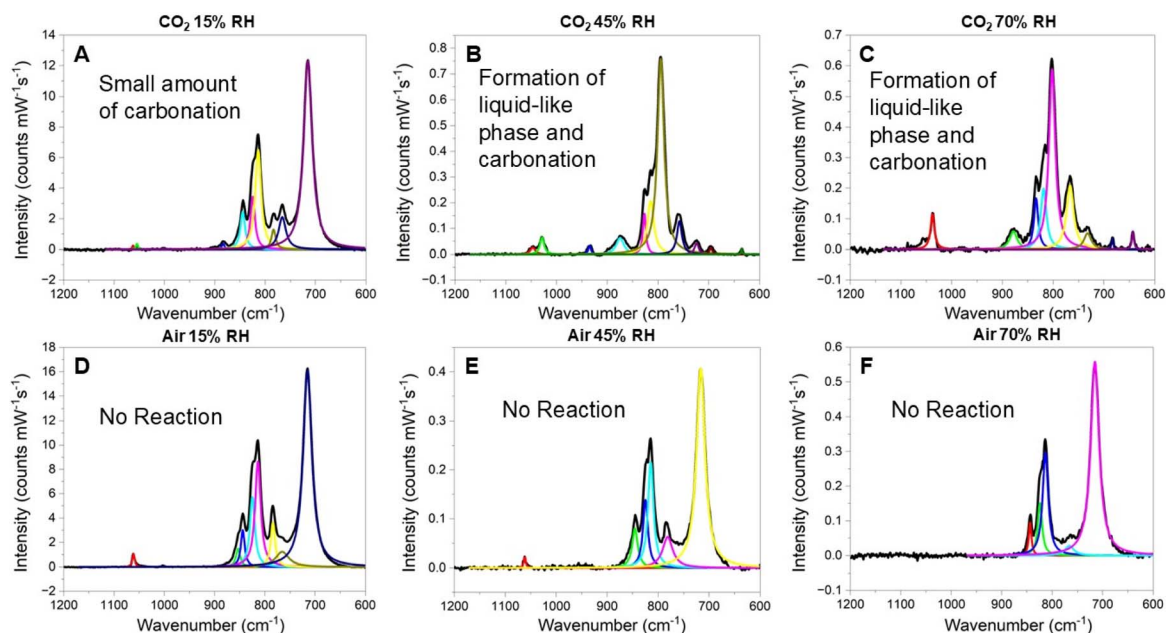


Fig. 5 Vibrational spectra following flow-through studies with KUT exposed to pure CO₂ at (A) 15%, (B) 45% and (C) 70% RH. Vibrational spectra of KUT following exposure to compressed air at 15%, 45% and 70% RH are shown as (D), (E), and (F), respectively.



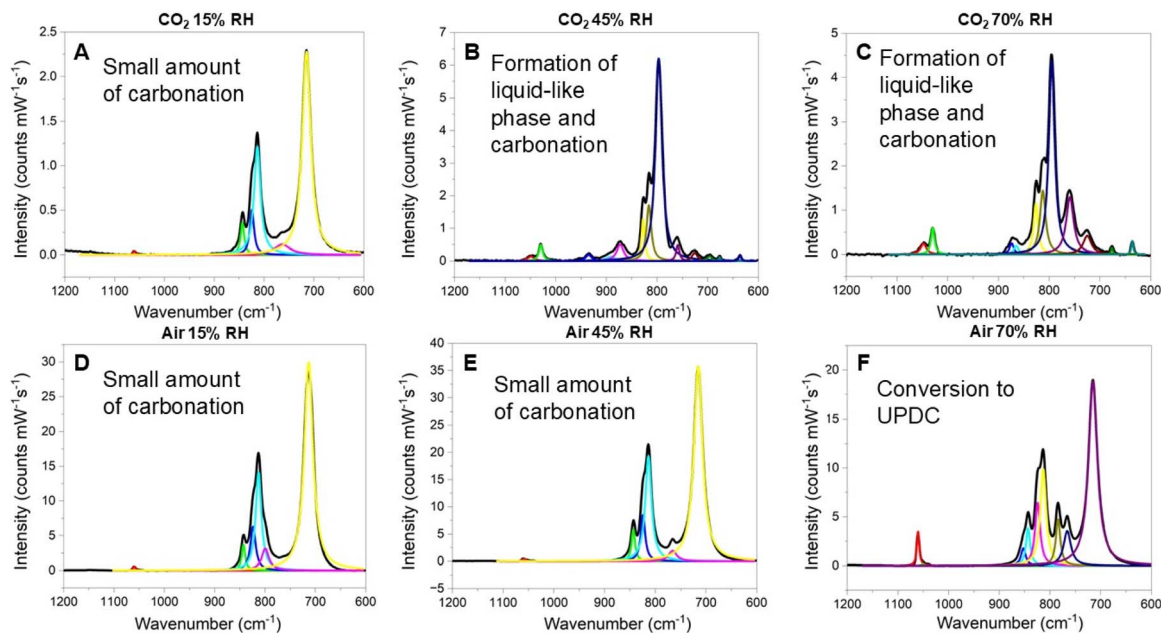


Fig. 6 Vibrational spectra following flow-through studies with KUPS exposed to pure CO₂ at (A) 15%, (B) 45% and (C) 70% RH. Vibrational spectra of KUPS following exposure to compressed air at 15%, 45% and 70% RH are shown as (D)–(F), respectively.

phases representing various stages in the carbonation reaction including the starting material (PC1), intermediate phase (PC2) and fully converted (PC3) (Fig. 7a). Then analyzing the computed biplot, we can reference the loadings with specific experimental data (e.g., wavenumber). The biplot reveals which Raman features fall within the 95% confidence ellipsoid, meaning those wavenumbers are observed in all samples and not unique to a specific phase in the reaction. Points falling outside of the ellipsoid are thus significant to the spectra of corresponding loadings. These are identified as 728, 800, and 767 cm⁻¹ for PCs 1, 2 and 3 respectively. We can then note that the band at 800 cm⁻¹ occurs most often when there are other features associated with carbonate brine formation, whereas the feature at 728 cm⁻¹ is unreacted KUT-1 (specifically the U=O Raman active mode),³² and 767 cm⁻¹ is the formation of the K₄[UO₂(O₂)(CO₃)₂]·2.5H₂O phase (U=O vibrational mode).⁴⁰ Thus, for KUT-1 and KUPS-1, the material is minimally reactive under air or CO₂ at low relative humidities. Under higher relative humidities, the material forms a brine-like substance that then converts to the uranyl peroxo-carbonate forms after drying.

The second PCA iteration included samples from CO₂ and compressed air flow-through experiments with KUT and KUPS and K₄[UO₂(O₂)(CO₃)₂]·2.5H₂O. The resulting loadings plot (Fig. 7b) and biplot are largely consistent with the first PCA iteration in that three distinct phases of the carbonation reaction are highlighted. PC1 is again identified as the unreacted materials but corresponds to 716 cm⁻¹ due to the shift in the uranyl symmetric stretch within the pristine materials Raman spectra.³⁵ PC2 (767 cm⁻¹) is identified as the carbonated materials and PC3 (800 cm⁻¹) corresponds to carbonate brines. While the specific identifications of PC2 and PC3 are reversed

from the first PCA iteration, this does not affect the overall interpretation of the Raman data and is likely due to the lower intensities of the associated samples. The same conclusions are still drawn in that KUT and KUPS are minimally reactive under air or CO₂ at low relative humidities and form liquid-like carbonate brines under high relative humidity.

Flow rates and reaction kinetics

Influence of gas flow rate and exposure time. Since the transformation of KUT-1 to the potassium uranyl peroxo-carbonate is slower at atmospheric CO₂ concentrations, additional factors may be more pronounced under such conditions. As such, we first qualitatively assessed the influence of gas flow rate and exposure time on the reactivity of KUT-1 exposed to either the ambient conditions or within the flow through system. The Raman spectrum of KUT-1 under ambient conditions suggested some degree of carbonation in as little as 24 hours with a band appearing at 1052 cm⁻¹ (ESI, Fig. S32†). Additional bands were observed at 852, 844, 835, 784, 768, 717 and 691 cm⁻¹ and are well aligned with features observed in the earlier flow-through studies. Powder diffraction of the dried materials further revealed that the material is a mixed phase of KUT-1 and K₄[UO₂(O₂)(CO₃)₂]·2.5H₂O (ESI, Fig. S33†). Vibrational spectrum of KUT-1 exposed to constant air flow for approximately 24 hours reveals bands at 844, 825, 814, and a strong band at 716 cm⁻¹ associated with ν₁ UO₂²⁺ for KUT (ESI, Fig. S34†).³⁵ The Raman spectrum and diffraction pattern (ESI, Fig. S35†) are both consistent with KUT meaning the higher flow rate led to decomposition of the K⁺/H₂O₂ network in KUT-1 yielding the KUT phase. Therefore, the H₂O₂ in the crystalline lattice is reactive to the air but does not directly correlate with carbonation.



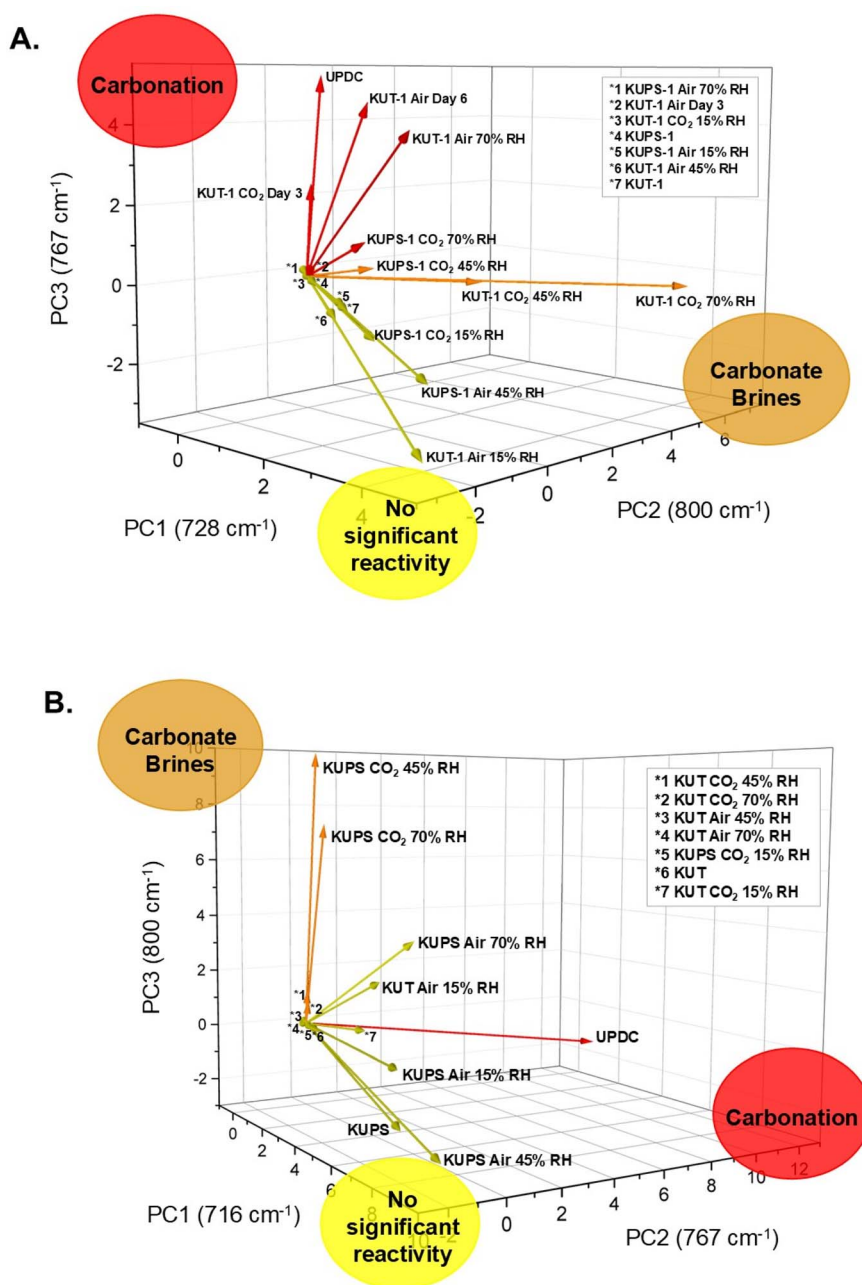


Fig. 7 Principal component analysis (PCA) of the Raman data for (A) KUT-1 and KUPS-1, and (B) KUT and KUPS. PC analysis reveals trends in reactivity of these phases under varying relative humidity and [CO₂] conditions and indicate no significant reactivity in low RH and/or low [CO₂] environments, transformation to carbonate brines under high RH conditions, and transformation to uranyl peroxy-carbonate (UPDC) under mid-high RH environments. The three distinct phases are correlated to the presence of specific Raman features at 728(A)/716(B) cm⁻¹ (no significant reactivity), 800 cm⁻¹ (carbonate brines), and 767 cm⁻¹ (carbonation).

Previous studies have identified that the carbonation reaction of both potassium uranyl triperoxide and potassium uranyl diperoxo superoxide are thermodynamically favorable,^{32,52} though details of the reaction kinetics have not been reported. As such, carbonation kinetics were determined for the reaction of the solid-state materials (KUT-1, KUPS-1, KUT and KUPS) with atmospheric CO₂. The kinetic data were modeled to four adsorption models and referenced to the carbonation kinetics for potassium superoxide (KO₂) pellets reported by Chegeni

*et al.*⁵³ (Table 2 and ESI Fig. S36–S55[†]). Based upon the *R*² values, carbonation for each of the four systems best follows second-order kinetics. The second order model assumes adsorption rate is dependent on chemisorption meaning the chemical reaction between the solid material and CO₂ drives the rate of carbonation.⁵⁴ The experimental data also fits well to the first-order model, which could indicate that the carbonation reaction for all systems follows pseudo-first-order kinetics. The Elovich^{55,56} and Richie second-order⁵⁷ models consistently



Table 2 Kinetic model parameters for the carbonation reaction of KUT-1, KUPS-1, KUT, KUPS (this work) and KO₂ pellets.⁵³

Kinetic model	Nonlinear form	Parameter	KUT-1	KUPS-1	KUT	KUPS	KO ₂
First-order	$q_t = q_c(1 - e^{-k_1 t})$	k_1	0.094	0.455	1.221	1.839	0.0324
		R^2	0.978	0.959	0.998	0.992	0.9348
Second-order	$q_t = k_2 \times q_c t \frac{1}{1 + k_2 \times q_c \times t}$	k_2	2.195×10^{-6}	8.441×10^{-6}	1.107×10^{-4}	1.310×10^{-4}	3.3×10^{-4}
		R^2	0.993	0.992	0.986	0.998	0.9633
Elovich	$q_t = \beta \times \log(\alpha \times \beta) + \beta \log(t)$	α	2.173×10^7	1.572×10^8	4.067×10^5	6.627×10^8	0.0279
		R^2	0.777	0.851	0.937	0.883	0.9763
Ritchie second-order	$q_t = q_c \frac{1}{1 + k_2 \times 2}$	k_2	0.249	3.796	7.116	13.902	348.63
		R^2	0.912	0.782	0.921	0.928	0.5656
Rate controlling	$q_t = k_{id} \times t^{0.5}$	k_{id}	43.245	60.282	128.171	97.610	2.1639
		R^2	0.956	0.991	0.985	0.957	0.9849

resulted in the lowest R^2 values. The former is used to describe adsorption onto heterogeneous surfaces, while the latter describes the adsorption of gases at vacant surface sites on a solid. Behind the first and second-order models, the data fits decently well with the rate controlling model which indicates intraparticle diffusion of the adsorbate through the pores of the adsorbent.^{56,58,59} Bulk diffusion likely has some effect on the carbonation reaction, however chemisorption appears to be the driving force behind the reaction kinetics.

Rate constants from the first- and second-order models reveal multiple trends regarding the carbonation reaction of the four systems. First, KUT-1 and KUPS-1 exhibit considerably slower kinetics compared to KUT and KUPS. This offers further support that the H₂O₂ in the crystalline lattice of KUT-1 and KUPS-1 is not directly correlated to the carbonation reaction. Additionally, the phases containing O₂^{•-} at the onset of air exposure (KUPS-1 and KUPS) were kinetically faster than their triperoxide analogues (KUT-1 and KUT). Only trace amounts of peroxide oxidation occur in the bulk solid meaning the O₂^{•-}-containing uranyl monomers exist as defects within the material. Despite forming in such small quantities, the presence of O₂^{•-} directly influences reactivity of the bulk. This explains why the second-order rate constant for KO₂ pellets is slightly larger than the constants reported in this study, as the O₂^{•-} concentration within KO₂ is higher than in the uranyl diperoxo superoxide materials; though, the slightly higher relative humidity utilized for those studies could have also contributed to faster kinetics.⁵³ The reaction kinetics demonstrate enhanced carbonation by uranyl diperoxo superoxide relative to uranyl triperoxide and are consistent with literature reports of enhanced carbon capture with O₂^{•-} containing materials.^{21,24,53}

Conclusion

Herein, we have reported optimal conditions promoting the carbonation of potassium uranyl triperoxide and potassium uranyl diperoxo superoxide phases within a flow-through system at 22 °C. Carbonate formation was monitored *via* Raman spectroscopy and elemental analysis. Flow-through studies under pure CO₂ revealed conversion to the uranyl peroxo-carbonate phase when relative humidity is at least 45%. Subsequent flow-through studies under compressed air reveal additional factors influencing the carbonation reaction,

including CO₂ concentration, gas flow rate, and the presence of O₂^{•-}. Further, flow-through studies in which the triperoxide starting materials were exposed to compressed air revealed the formation of O₂^{•-} but no initial carbonation, suggesting that oxidation of O₂^{•-} to O₂^{•-} is an early step in the reaction mechanism. These findings were reflected in the reaction kinetics of solid-state KUT-1, KUPS-1, KUT and KUPS with atmospheric CO₂, which follow pseudo first-order kinetics. Notably, these studies found that the carbonation of U(vi) diperoxo superoxide phases are more kinetically favorable than their analogous U(vi) triperoxide phases.

Overall, this study demonstrates conditions, namely relative humidity and presence of O₂^{•-} within the adsorbent, which promote the transformation of uranyl peroxide materials to uranyl carbonate phases *via* CO₂ removal from ambient air. Our findings present a more efficient sorbent than recently reported transition metal (*e.g.*, vanadium) peroxides in terms of uptake capacity and reaction kinetics, provided for by the ability of U(vi) to stabilize ROS long enough to allow for reaction with CO₂. Further, our findings provide insight into the carbonation reaction mechanism, but additional efforts are ongoing to identify specific mechanistic steps for this process. While the current study shows enhanced reactivity for the solid-state potassium uranyl diperoxo superoxide materials, we acknowledge that their reactivity in solution is unknown. Additional studies are therefore necessary to evaluate the carbonation reaction of these materials in solution to determine the possible catalytic nature of these materials within strong base DAC processes.

Data availability

The data supporting this article have been included as part of the ESI.†

Conflicts of interest

There are no conflicts to declare.

Acknowledgements

This work was supported by the U.S. Department of Energy Basic Energy Sciences (DE-SC0023479). We acknowledge the



University of Iowa Materials Analysis, Testing and Fabrication Facility, Dr Daniel Unruh for support associated with the X-ray diffractometer and Raman spectrometer, and Dr Michael Sinnwell for support associated with the elemental analyzer.

References

- 1 A. Allangawi, E. F. H. Alzaimoor, H. H. Shanaah, H. A. Mohammed, H. Saqer, A. A. El-Fattah and A. H. Kamel, *C*, 2023, **9**, 17–46.
- 2 D. M. D'Alessandro, B. Smit and J. R. Long, *Angew. Chem., Int. Ed.*, 2010, **49**, 6058–6082.
- 3 C. Hepburn, E. Adlen, J. Beddington, E. A. Carter, S. Fuss, N. Mac Dowell, J. C. Minx, P. Smith and C. K. Williams, *Nature*, 2019, **575**, 87–97.
- 4 E. S. Sanz-Pérez, C. R. Murdock, S. A. Didas and C. W. Jones, *Chem. Rev.*, 2016, **116**, 11840–11876.
- 5 M. Ozkan, S. P. Nayak, A. D. Ruiz and W. Jiang, *iScience*, 2022, **25**, 103990.
- 6 K. Lackner, H.-J. Ziock and P. Grimes, Report number: LA-UR-99-583, United States, 1999.
- 7 S. A. Didas, S. Choi, W. Chaikittisilp and C. W. Jones, *Acc. Chem. Res.*, 2015, **48**, 2680–2687.
- 8 A. Goepfert, H. Zhang, M. Czaun, R. B. May, G. K. S. Prakash, G. A. Olah and S. R. Narayanan, *ChemSusChem*, 2014, **7**, 1386–1397.
- 9 L. B. Hamdy, C. Goel, J. A. Rudd, A. R. Barron and E. Andreoli, *Mater. Adv.*, 2021, **2**, 5843–5880.
- 10 X. Shi, H. Xiao, H. Azarabadi, J. Song, X. Wu, X. Chen and K. S. Lackner, *Angew. Chem., Int. Ed.*, 2020, **59**, 6984–7006.
- 11 E. Unveren, B. Monkul, Ş. Sariođlan, N. Karademir and E. Alper, *Petroleum*, 2016, **3**, 37–50.
- 12 M. Mahmoudkhani and D. W. Keith, *Int. J. Greenhouse Gas Control*, 2009, **3**, 376–384.
- 13 A. A. H. I. Mourad, A. F. Mohammad, M. Altarawneh, A. H. Al-Marzouqi, M. H. El-Naas and M. H. Al-Marzouqi, *Int. J. Energy Res.*, 2021, **45**, 13952–13964.
- 14 R. Sen, A. Goepfert, S. Kar and G. K. S. Prakash, *J. Am. Chem. Soc.*, 2020, **142**, 4544–4549.
- 15 S. Kar, A. Goepfert, V. Galvan, R. Chowdhury, J. Olah and G. K. S. Prakash, *J. Am. Chem. Soc.*, 2018, **140**, 16873–16876.
- 16 M. Saeidi, A. Ghaemi, K. Tahvildari and P. Derakhshi, *J. Chin. Chem. Soc.*, 2018, **65**, 1465–1475.
- 17 P. Smith, S. Davis, F. Creutzig, S. Fuss, J. Minx, B. Gabrielle, E. Kato, R. Jackson, A. Cowie, E. Kriegler, D. Vuuren, J. Rogelj, P. Ciais, J. Milne, J. Canadell, D. McCollum, G. Peters, R. Andrew, V. Krey and C. Yongsung, *Nat. Clim. Change*, 2015, **6**, 42–50.
- 18 G. Leonzio, P. S. Fennell and N. Shah, *Appl. Sci.*, 2022, **12**, 2618.
- 19 X. Zhang, Z. Song, R. Gani and T. Zhou, *Ind. Eng. Chem. Res.*, 2020, **59**, 2005–2012.
- 20 X. Lan and R. Keeling, <https://gml.noaa.gov/ccgg/trends/data.html>, accessed April 2025.
- 21 U. Stoin, Z. Barnea and Y. Sasson, *RSC Adv.*, 2014, **4**, 36544–36552.
- 22 J. S. Hirschi, M. Nyman and T. J. Zuehlsdorff, *J. Phys. Chem. A*, 2024, **128**, 7785–7794.
- 23 E. G. Ribó, Z. Mao, J. S. Hirschi, T. Lindsay, K. Bach, E. D. Walter, C. R. Simons, T. J. Zuehlsdorff and M. Nyman, *Chem. Sci.*, 2024, **15**, 1700–1713.
- 24 E. Shirman and Y. Sasson, *Greenhouse Gases:Sci. Technol.*, 2024, **14**, 1037–1048.
- 25 H. T. Lin, Y. C. Chao, H. W. Hsu, C. A. Chen, G. B. Chen and F. H. Wu, *presented in part at the ASPACC 2019*, Fukuoka, Japan, 2019.
- 26 B. Yu, B. Zou and C.-W. Hu, *J. CO₂ Util.*, 2018, **26**, 314–322.
- 27 V. Kumar, N. Kumar Lamba, A. Baig, A. Kumar Sonker, N. Sharma, J. Kaushik, K. Malika Tripathi, Sonal and S. Kumar Sonkar, *Chem. Eng. J.*, 2024, **500**, 156786.
- 28 Z. Mao, M. Rashwan, E. Garrido Ribó, M. Nord, L. N. Zakharov, T. W. Surta, A. Uysal and M. Nyman, *J. Am. Chem. Soc.*, 2024, **146**, 19489–19498.
- 29 K. Bach, E. Garrido Ribó, J. S. Hirschi, Z. Mao, M. T. Nord, L. N. Zakharov, K. A. Goulas, T. J. Zuehlsdorff and M. Nyman, *Chem. Mater.*, 2025, **37**, 48–61.
- 30 M. Fairley, G. E. Sigmon and J. A. LaVerne, *Inorg. Chem.*, 2023, **62**, 19780–19785.
- 31 Z. C. Emory, J. A. LaVerne and P. C. Burns, *Dalton Trans.*, 2024, **53**, 17169–17178.
- 32 D. V. Kravchuk, N. N. Dahlen, S. J. Kruse, C. D. Malliakas, P. M. Shand and T. Z. Forbes, *Angew. Chem., Int. Ed.*, 2021, **60**, 15041–15048.
- 33 D. V. Kravchuk and T. Z. Forbes, *Angew. Chem., Int. Ed.*, 2019, **58**, 18429–18433.
- 34 S. K. Scherrer, H. Rajapaksha, D. V. Kravchuk, S. E. Mason and T. Z. Forbes, *Chem. Commun.*, 2024, **60**, 10584–10587.
- 35 M. Dembowski, V. Bernales, J. Qiu, S. Hickam, G. Gaspar, L. Gagliardi and P. C. Burns, *Inorg. Chem.*, 2017, **56**, 1574–1580.
- 36 K. An, A. Farooqui and S. T. McCoy, *Appl. Energy*, 2022, **325**, 119895.
- 37 Y. Gao, Y. Tao, G. Li, P. Shen, R. J. M. Pellenq and C. S. Poon, *Proc. Natl. Acad. Sci. U. S. A.*, 2025, **122**, e2418239121.
- 38 M. Hayyan, M. A. Hashim and I. M. AlNashef, *Chem. Rev.*, 2016, **116**, 3029–3085.
- 39 R. A. Zehnder, S. M. Peper, B. L. Scott and W. H. Runde, *Acta Crystallogr., Sect. C:Cryst. Struct. Commun.*, 2005, **61**, i3–i5.
- 40 G. Goff, L. Brodnax, M. Cisneros, S. Peper, S. Field, B. Scott and W. Runde, *Inorg. Chem.*, 2008, **47**, 1984–1990.
- 41 H. Abdi and L. J. Williams, *WIREs Computational Statistics*, 2010, **2**, 433–459.
- 42 L. Zhang and P. A. Lay, *Inorg. Chem.*, 1998, **37**, 1729–1733.
- 43 H. H. Eysel and S. Thym, *Z. Anorg. Allg. Chem.*, 1975, **411**, 97–102.
- 44 A. R. Davis and B. G. Oliver, *J. Solution Chem.*, 1972, **1**, 329–339.
- 45 J. D. Frantz, *Chem. Geol.*, 1998, **152**, 211–225.
- 46 B. G. Oliver and A. R. Davis, *Can. J. Chem.*, 1973, **51**, 698–702.
- 47 A. Anderson, C. Chieh, D. E. Irish and J. P. K. Tong, *Can. J. Chem.*, 1980, **58**, 1651–1658.
- 48 R. L. Frost and J. Čejka, *J. Raman Spectrosc.*, 2007, **38**, 1488–1493.



- 49 R. L. Frost and J. Čejka, *J. Raman Spectrosc.*, 2009, **40**, 1096–1103.
- 50 G. Mestl, M. P. Rosynek and J. H. Lunsford, *J. Phys. Chem. B*, 1998, **102**, 154–161.
- 51 G. Lu, A. J. Haes and T. Z. Forbes, *Coord. Chem. Rev.*, 2018, **374**, 314–344.
- 52 A. Arteaga, T. Arino, G. C. Moore, J. L. Bustos, M. K. Horton, K. A. Persson, J. Li, W. F. Stickle, T. A. Kohlgruber, R. G. Surbella III and M. Nyman, *Chem.–Eur. J.*, 2024, **30**, e202301687.
- 53 A. Chegeni, V. Babaeipour, M. Fathollahi and S. G. Hosseini, *J. Cluster Sci.*, 2022, **33**, 2167–2178.
- 54 S. M. Lalji, M. Ayubi, S. I. Ali, S. u. Rahman and M. Mustafa, *Discover Chemistry*, 2024, **1**, 71.
- 55 A. N. Ebelegi, N. Ayawei and D. Wankasi, *Open J. Phys. Chem.*, 2020, **10**, 166–182.
- 56 A.-B. Al-Odayni, F. S. Alsubaie, N. A. Y. Abdu, H. M. Al-Kahtani and W. S. Saeed, *Polymers*, 2023, **15**, 1983–2001.
- 57 A. G. Ritchie, *J. Chem. Soc., Faraday Trans. 1*, 1977, **73**, 1650–1653.
- 58 E. Asuquo, A. Martin, P. Nzerem, F. Siperstein and X. Fan, *J. Environ. Chem. Eng.*, 2017, **5**, 679–698.
- 59 E. Guibal, C. Milot and J. M. Tobin, *Ind. Eng. Chem. Res.*, 1998, **37**, 1454–1463.

